

Numerical Analysis of the Effect of Pile Tip Shape on Soil Behavior around Pile

Y. Wu¹ and H. Yamamoto²

¹Graduate School for International Development and Cooperation, Hiroshima University, Higashi-Hiroshima, Japan

²Graduate School for International Development and Cooperation, Hiroshima University, Higashi-Hiroshima, Japan

E-mail: yangwu0226@hotmail.com

ABSTRACT: Underreamed (enlarged-base) piles are commonly employed in engineering practice. The pile tip is often made into different shapes. This study analyzes the effects of various underreamed pile tip shapes on the soil behavior around the pile. A finite element analysis combined with a mixed incremental method for the updated Lagrangian method is presented using a small strain formulation to solve the large deformation problem. Constitutive model for sand with particle crushing and joint elements are used to represent the behavior of sand around the pile and the interactive surface between the sand and the pile. The predicted relationship between the normalized bearing stress and displacement are compared with experimental measurements, showing good agreement. The numerical results demonstrate that the distributed area of the high-value radial stress contour and the high-value vertical stress decrease as the pile tip gets sharper. The distributed areas of the high positive-value vertical strain, the high negative-value radial strain and the high negative-value circumferential strain expand as the pile tip gets sharper. The numerical results clearly indicate that the soil beneath the pile tip at different depths displays various volumetric changes and confirms the necessity of the constitutive model for sand with particle crushing.

Keywords: Model pile, particle crushing, large deformation theory, joint element, pile tip shape.

1. INTRODUCTION

The behavior of piles remains one of the largest sources of uncertainty in geotechnical engineering. Much of the uncertainty is because of a lack of understanding of the physical mechanism that controls the characteristics of deformation, strain and stress in the soil during pile installation and loading. In some installations, the pile base is enlarged to improve its ultimate bearing capacity. Considerable effort has been devoted to the investigation of the bearing capacity of model piles with enlarged pile bases or shaft diameters by Cooke and Whitaker (1961), Martin and Destephens (1983), Kim *et al.* (2007), Ishikawa *et al.* (2011) and Ishikawa *et al.* (2012). To date, the most fundamental and convincing aspects of pile design still rely on experiments and experience.

In the past thirty years, tremendous progress has been made in the numerical analysis of pile foundations. For example, finite element method (FEM) is a time-saving and flexible tool compared to traditional experience-based methods. However, the numerical analysis of pile loading is generally challenging because the soil-structure interaction system involving large deformations is complicated. Many researchers have attempted to solve the pile loading and penetration problem using large deformation theory. Kioussis *et al.* (1988) has proposed the large deformation theory and the application of cone penetration. Hu and Randolph (1998a) and Hu and Randolph (1998b) have presented a practical approach, the arbitrary Lagrangian Eulerian (ALE) method, to solve large deformation problems, such as the bearing capacity of footing using the well-established small-strain finite element code. Sheng *et al.* (2005) and Sheng *et al.* (2009) have initially adopted the friction slip method and frictional element to tackle deep penetration and the soil-pile contact problem. Nazem *et al.* (2006), Nazem *et al.* (2008), Nazem *et al.* (2009) and Nazem *et al.* (2010) have presented the arbitrary Lagrangian Eulerian method combined with adaptive computation technology to analyze large deformations in geomechanics, extending these strategies to consolidation and dynamic problems. Recently, Qiu *et al.* (2011a), Qiu and Henke (2011b) and Qiu and Grade (2012) have employed the coupled Eulerian Lagrangian (CEL) method to investigate the spudcan pile foundation penetration in loose sand overlying on weak clay. Vavourakis *et al.* (2013) have discussed remeshing and remapping technologies for large deformation analysis. In addition, a deep and comprehensive understanding of the pile bearing mechanism cannot be realized without considering the soil-pile interaction. Progressive shearing failure occurs at the interface, where significant high stresses and strains are transmitted. Gennaro *et al.* (2008) and Said

et al. (2009) have performed a finite element analysis of piles loading in sand with a mechanical elasto-plastic interface element.

The strength reduction of soil after crushing should also be considered when estimating the bearing capacity of the pile. Some soil particles around the pile tip tend to be crushed when the external force exceeds their crushing strength. It is necessary to employ a suitable constitutive model to represent soil behavior in high compression stress regions. Simonini (1996) has investigated the behavior of dense sand around the pile tip in the particle crushing region using the finite element method. That study found that two factors, relative density and mean effective stress level, influenced sand particle crushing. Yasufuku and Hyde (1995) and Yasufuku *et al.* (2001) have proposed the calculation formulation for pile end-bearing capacity by incorporating a factor for particle crushing. The cavity expansion theory for the bearing capacity of the pile was analyzed in terms of the compressibility factor, the friction angle and the average volumetric strain and shear stiffness. Keji *et al.* (2009) has performed the pile loading test into three kinds of sand, observed the behavior of sand around pile tip and modified the bearing capacity factor. Yang *et al.* (2006), Yang and Mu (2008) and Yu and Yang (2012) have investigated the end-bearing capacity of the pile in sand using the concept of state-dependent strength.

There exists very limited research on the effect of pile tip shape on the behavior of the surrounding soil. Lobo-Guerrero and Vallejo (2007) remarked that pile tip shape has a significant impact on pile penetration and particle crushing. The current study analyzes the effect of the pile tip shape on the bearing mechanism of the pile and the mechanical behavior of the sand around the pile. This paper presents a finite element analysis of piles with different pile tip shapes and under different surcharge pressures. In previous large deformation analyses of the pile-loading problem, soil behavior is represented by a simple constitutive model, as in Sheng *et al.* (2008). This numerical study integrates the constitutive model for sand with particle crushing with the finite element analysis using large deformation theory. A mixed incremental method for the updated Lagrangian method by Chen and Mizuno (1990) is used in the finite element analysis to solve the large deformation problem. To better simulate the interface behavior, a zero-thickness joint element, simulating the soil-pile interaction, is employed in the finite element analysis. The relationship between the normalized bearing stress and displacement is estimated, and the soil deformation around the pile is predicted. The numerical results of the relationship between the stress ratio and the volumetric variance at different depths beneath the pile tip are also presented.

2. MODEL PILE LOADING TESTS

Underreamed piles are usually used to increase the size of the pile base diameters and hence provide greater bearing capacity at a more economical cost than a straight-shaft pile. A modified form, the pencil-shaped base pile, can effectively prevent cracks from occurring in the enlarged base. In the model pile loading tests conducted by Yamamoto *et al.* (2003), straight piles and underreamed piles with the same shaft diameter, i.e., 30 mm, were tested. The underreamed piles included flat base piles and the pencil-shaped base piles, as shown in Figure 1. The base-enlarged part, with a diameter 54 mm, was constructed of mortar. The convergent angle α , which is between the axial line and the line of the pile base, is used to describe the shape of the pile base. The model piles were tested at convergent angles α of 30, 60 and 90 degrees.

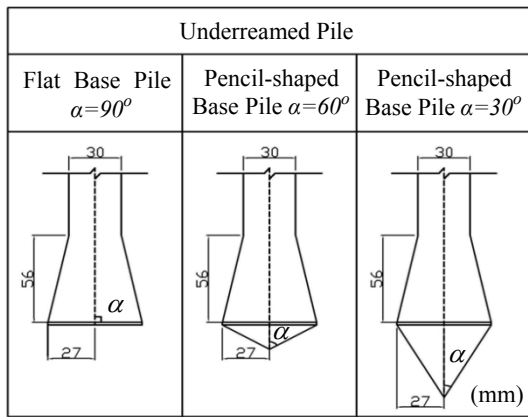


Figure 1 Different types of pile tip

The model piles with different pile base shapes were jacked into a ground tank container filled with Toyoura sand to demonstrate the effects of pile base shape and surcharge pressure level on the bearing capacity and to investigate the movement of sand particles around the pile tip area. The test setup is shown in Figure 2. The setup consisted of the ground tank container, the loading installation and the measurement device. The ground tank container was 600 mm in height and 584.2 mm in diameter. The diameter of the steel model pile was 30 mm, and the diameter of the enlarged pile base was 54 mm. The diameter ratio of the ground tank container to the steel model pile was deliberately adjusted to reduce any effects from the interior surface of the ground tank container. Toyoura sand was poured into the ground tank container layer by layer to ensure that it was well-distributed and homogeneous after the prior installation of the model pile.

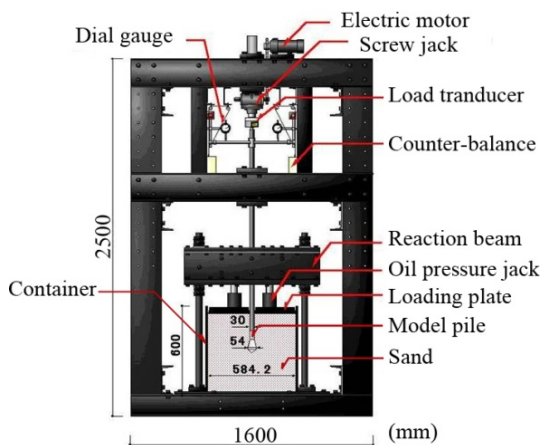


Figure 2 The testing apparatus

The relative density of dry, dense, uniform Toyoura sand is approximately 90%. Toyoura sand is one kind of uniform fine sand with mainly sub-angular particle shape. The physical and material properties of Toyoura sand are given in Table 1. Teflon sheets were attached to the interface between the ground tank container and the Toyoura sand and between the model pile and the Toyoura sand using silicon grease to eliminate the effect of frictional force. The penetration depth of the model pile and the load cell on the pile head were recorded by a data logger and computer.

Table 1 Physical properties of Toyoura sand

Mean grain size (mm)	0.20
Coefficient of uniformity	1.21
Specific gravity	2.656
Minimum dry density (g/cm ³)	1.332
Maximum dry density (g/cm ³)	1.646
Relative density (%)	90
Internal friction angle(degree)	44.0

Model pile loading tests were performed by a displacement-controlled method. The penetrating speed of the model pile into the sand layer was 0.5 mm/min. The final displacement of the model pile was equal to the diameter of the pile shaft. Three levels of surcharge pressure, 200 kPa, 400 kPa and 600 kPa, were directly applied on the upper surface of the model ground to simulate the actual soil stresses at different depths.

The occurrence of particle crushing was confirmed by comparing the grain size distribution curves of Toyoura sand before and after the model tests, as measured by Li and Yamamoto (2005). The sand around the pile tip was carefully removed after loading and processed for the sieve analysis test. The region used for the analysis was a cubic column with a pile diameter equal to the side length just beneath the pile tip. The characteristics of the model ground material and the conditions of axisymmetric loading in Li's experiment are identical to the current study. It is believed that particle crushing occurs in the current model underreamed pile loading test as well.

3. NUMERICAL ANALYSIS METHOD

It is important to consider the geometrical nonlinearity caused by the large deformation to establish a model of the actual behavior of the structure. More accurate and reliable numerical solutions are obtained and provide insight into the essence of the problem. The deformation of soil under complex stresses in the soil surrounding the pile tip exhibits typical large deformation behavior. Therefore, finite element analysis using large deformation theory is an effective approach to tackle the driving and penetrating pile process.

Generally, total Lagrangian (TL) and updated Lagrangian (UL) methods are regarded as the two primary technologies for solving large deformation problems in geomechanics. The major difference between these two methods is the reference configuration employed. The TL method refers to the initial configuration, while the UL method chooses to refer to the current configuration. The two methods are not two different solutions to the problem but rather two different approaches to the equilibrium equations. They can be linked logically and mathematically. However, the UL method is more versatile and has gained popularity over the TL method. Hibbitt *et al.* (1970) reviewed the history of large deformation and strain and derived an incremental stiffness equation of the finite element method in a Lagrangian frame of reference. In recent years, ALE and CEL methods have been positively adopted and popularized in succession. However, these two methods are complicated because of the intricate nature of the remeshing and adaptive process.

The expression of the Jaumann stress ratio increment, $d\sigma_{ij}^J$, adopted by Chen and Mizuno (1990), combined with the virtual work, enables the conventional finite element method to solve for large deformation behavior with small deformation and strain theory. In that case, the stress and strain integration can also be performed using a method similar to the small deformation method. Consequently, the mixed incremental method for the UL method is employed in this study. Its description is reviewed in the following.

The state variables are assumed to satisfy the equilibrium condition from the initial time 0 to time t . The general expression of the virtual work at some intermediate time t is written in Eq. (1) as follows:

$$\int_A T_i^t \delta(du_i) dA^t + \int_V \rho^t F_i^t(x_j) \delta(du_i) dV^t = \int_V \sigma_{ij}^t \delta(d\varepsilon_{ij}) dV^t \quad (1)$$

where T is the traction force, u is the displacement, F is the body force per unit mass, ρ is the mass density of the initial state, δ is a virtual value, σ_{ij} is the Cauchy stress tensor and ε_{ij} is the infinitesimal strain tensor. The state variables with superscript t denote the variables at intermediate time t .

$$R^{t+dt} = \int_{V^t} \sigma_{ij}^{t+dt} \delta\varepsilon_{ij}^{t+dt} dV^{t+dt} \quad (2)$$

where R is the external work by the body force and traction force. The major difficulty in solving the large deformation and strain problem is determining the configuration in time $t+dt$. To solve Eq. (2), all state variables must be linked to a known configuration at time t . The UL method employs the current configuration at time $t+dt$, while the TL method refers to the initial configuration at time 0 . Here, only the UL method is explained.

Once the deformation of a structure becomes large during loading, the Cauchy stress tensor and strain tensor no longer apply. It is therefore necessary to adopt appropriate expressions of stress and strain to solve the large deformation problem. The equation can be transformed to the current configuration at time t as follows:

$$\delta W_{ext} = \int_V \sigma_{ij}^{t+dt} \delta\varepsilon_{ij}^{t+dt} dV = \int_{\hat{V}} S_{ij}^{t+dt} \delta E_{ij}^{t+dt} d\hat{V} \quad (3)$$

The external virtual work, δW_{ext} , at time $t+dt$ can be expressed in terms of either the Cauchy stress tensor σ_{ij} and the infinitesimal strain increment tensor $\delta\varepsilon_{ij}$ or the second Piola-Kichhoff stress, S_{ij} , and the Lagrangian strain increment tensor, δE_{ij} , in Eq. (3), where \hat{V} and V are the volume at the initial and current state, respectively. The Lagrangian strain incremental tensor is obtained from the difference of the Lagrangian strain at time $t+dt$ and t in Eq. (4) and specifically given by Eq. (5) as follows:

$$dE_{ij} = E_{ij}^{t+dt} - E_{ij}^t \quad (4)$$

$$dE_{ij} = \frac{1}{2}(du_{i,j} + du_{j,i} + du_{k,i} du_{k,j}) \quad (5)$$

The subscript after the comma is the partial derivative with respect to the coordinate X_i in the initial configuration. The coordinate system in the initial (X_i) configuration and current (x_i) configuration are related by the displacement vector as $x_i = X_i + u_i$.

$$du_{i,j} = d\varepsilon_{ij} + d\Omega_{ij} \quad (6)$$

$$d\Omega_{ij} = (u_{i,j} - u_{j,i})/2 \quad (7)$$

where $du_{i,j}$ is comprised of the Cauchy strain tensor and spin tensor in Eq. (6), $d\varepsilon_{ij}$ is the Cauchy strain for infinitesimal strain and $d\Omega_{ij}$ is spin tensor from Eq. (7). Inserting the Eq. (6) and Eq. (7) into the Eq. (5) results in the Eq. (8) as follows:

$$dE_{ij} = d\varepsilon_{ij} + \frac{1}{2}(d\varepsilon_{ki} + d\Omega_{ki})(d\varepsilon_{kj} + d\Omega_{kj}) \quad (8)$$

In the external work equation, the stress and strain tensors always appear in pairs. The companion stress expression that often appears with the Lagrangian strain tensor is the second Piola-Kirchhoff stress tensor, S_{ij} , as follows:

$$S_{ij}^{t+dt} = S_{ij}^t + dS_{ij} = \sigma_{ij}^t + dS_{ij} \quad (9)$$

The second Piola-Kirchhoff stress at the time $t+dt$ in Eq. (9) is equivalent to the second Piola-Kirchhoff stress at time t plus its incremental value, as follows:

$$d\sigma_{ij} = d\sigma_{ij}^J + \psi_{ijkl} d\varepsilon_{kl} \quad (10)$$

where ψ_{ijkl} is expressed in terms of the current stress and accounts for the effects of the rigid body motion. The Jaumann stress tensor increment, $d\sigma_{ij}^J$, employed by Chen and Mizuno (1990), is related to the Cauchy stress tensor increment, $d\sigma_{ij}$, in Eq. (10).

The term $d\tau_{ij}$ is the incremental Cartesian stress tensor for the subsequent configuration, referred to a local coordinate. It is identical to the Jaumann stress tensor increment, $d\sigma_{ij}^J$, as follows:

$$d\tau_{ij} = D_{ijkl}^{ep} d\varepsilon_{kl} \quad (11)$$

where, D_{ijkl}^{ep} is the elastic-plastic constitutive tensor expressed in terms of the Cauchy stress tensor. The Cauchy stress tensor increment, $d\sigma_{ij}$, is assumed, as shown by Gadala *et al.* (1984), to be equal to the second Piola-Kirchhoff stress increment dS_{ij} . Combining Eq. (9), Eq. (10) and Eq. (11) yields Eq. (12), an expression for the second Piola-Kirchhoff stress at time $t+dt$, as follows:

$$S_{ij}^{t+dt} = \sigma_{ij}^t + (C_{ijkl}^{ep} + \psi_{ijkl}) d\varepsilon_{kl} \quad (12)$$

Inserting Eq. (12) and the incremental form of Eq. (5) into Eq. (3), the external virtual work expression in terms of the Cauchy stress and strain tensor is obtained in Eq. (13) as follows:

$$\begin{aligned} & \int_V \sigma_{ij} \left\{ d\varepsilon_{ki} \delta(d\varepsilon_{kj}) + d\varepsilon_{ki} \delta(d\Omega_{kj}) + d\Omega_{ki} \delta(d\varepsilon_{kj}) + d\Omega_{ki} \delta(d\Omega_{kj}) \right\} dV \\ & + \int_V (d\tau_{ij} + \psi_{ijkl} d\varepsilon_{kl}) \delta(d\varepsilon_{ij}) dV \\ & = \int_A (T_i + dT_i) \delta u_i dA + \int_V \rho_o \{ F_i(x_j + dF_i) \} \delta(du_i) dV - \int_V \sigma_{ij} \delta\varepsilon_{ij} dV \end{aligned} \quad (13)$$

For convenient integration using the finite element method, Eq. (13) has been transformed into the matrix formulation as Eq. (14). The first part on the left of the equilibrium equation is obtained by $\{d\varepsilon_L\} = [B_L] \{dU\}$, where $[B_L]$ is the transformation matrix from strain to displacement.

$$\left(\sum_V [B_L]^T [A] [B_L] dV + \sum_V [B_{NL}]^T ([D] + [\psi]) [B_{NL}] dV \right) \{dU\} = \{dR\} \quad (14)$$

where $\{dR\}$ is the external force vector, $\{dU\}$ is the displacement vector and $[\psi]$ and $[A]$ are the matrixes used in composition of the Cauchy stress, σ_{ij} , shown in Eq. (15) and Eq. (16) for the axially symmetric stress field. The terms for rigid body motion are included in Eq. (15). The constitutive matrix, $[D]$, is determined from the constitutive model for sand with particle crushing described in the next section.

$$[\psi] = \begin{bmatrix} -\sigma_{rr} & \sigma_{rr} & \sigma_{rr} & -\sigma_{rz} \\ \sigma_{zz} & -\sigma_{zz} & \sigma_{zz} & -\sigma_{rz} \\ \sigma_{\theta\theta} & \sigma_{\theta\theta} & -\sigma_{\theta\theta} & 0 \\ 0 & 0 & \sigma_{rz} & -\frac{1}{2}(\sigma_{rr} + \sigma_{zz}) \end{bmatrix} \quad (15)$$

Consequently, in this mixed incremental method for the updated Lagrangian method, the stress and strain integrations can be performed in a manner similar to that used for the small deformation problem.

$$[A] = \begin{bmatrix} \sigma_{rr} & 0 & 0 & \frac{1}{2}\sigma_{rz} & \sigma_{rz} \\ 0 & \sigma_{zz} & 0 & \frac{1}{2}\sigma_{rz} & -\sigma_{rz} \\ 0 & 0 & \sigma_{\theta\theta} & 0 & 0 \\ \frac{1}{2}\sigma_{rz} & \frac{1}{2}\sigma_{rz} & 0 & \frac{1}{4}(\sigma_{rr} + \sigma_{zz}) & \frac{1}{2}(\sigma_{zz} - \sigma_{rr}) \\ \sigma_{rz} & -\sigma_{rz} & 0 & \frac{1}{2}(\sigma_{zz} - \sigma_{rr}) & \sigma_{rr} + \sigma_{zz} \end{bmatrix} \quad (16)$$

4. NUMERICAL MODELLING

Simulating the pile loading and driving process is challenging because it involves both geometrical and material nonlinearities. The geometrical nonlinearity has been solved by the mixed incremental method. The difficulty in considering the material nonlinearity is from the modeling of the soil behavior around the pile and the model of the soil-pile interface.

4.1 Constitutive model and parameters

4.1.1 Constitutive model for sand with crushing

The region around the pile tip is concentrated with significant mean and deviatoric stresses. The importance of considering particle crushing when estimating the bearing capacity of the pile has been found by examining the change in properties before and after crushing by Vesic *et al.* (1968), Miura and Yamanouchi (1977), Miura *et al.* (1984), Hardin (1985), Fukumoto (1992) and Lade *et al.* (1996). Therefore, particle crushing should be reasonably simulated when pile loading in sand is studied.

The solution to pile loading in sand requires understanding and modeling the sand behavior under extremely high pressure. Many researchers have proposed comprehensive constitutive models incorporating particle crushing. Sun *et al.* (2007) modified the plastic hardening parameter to account for the effect of particle crushing. Daouadji *et al.* (2001) and Daouadji and Hicher (2010) proposed a constitutive model and its enhanced version including particle breakage, and proved their theory using laboratory tests. The grain distribution curve was chosen as the parameter in their model. Kikumoto *et al.* (2010) described particle crushing behavior with a revised SEVERN-TRENT sand model, on the strength of critical state theory. Hu *et al.* (2011) established relationships among internal energy, critical state line and particle crushing index.

Recently, Yao *et al.* (2008a) proposed a revised hardening parameter for the modified Cam Clay model, initially proposed by Roscoe and Burland (1968), to represent the dilatancy characteristic

of sand. The constitutive model proposed by Yao *et al.* (2008b) is capable of predicting the soil dilatancy from negative to positive under low confining pressure and only negative dilatancy under high confining pressure. In addition, the reduction of peak strength with increasing confining pressure is also reasonably represented. This model incorporates only seven parameters and its validity has been verified by Wu *et al.* (2013) to simulate sand behavior around pile. Therefore, it is positively adopted in this numerical analysis.

4.1.2 Dilatancy prediction and parameter determination

The prediction of dilatancy by this model is briefly explained in this section. The critical state curve, M_c , contains three curves that transform onto the p - q plane, as shown in Figure 3.

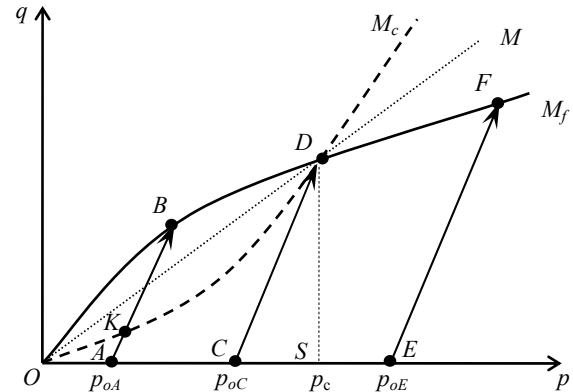


Figure 3 The curves of M_c and M_f and stress paths in p - q plane

The horizontal axis, p , indicates the mean stress, while the vertical axis, q , indicates the deviatoric stress. The characteristic state curve, M_c , is the boundary line of volume variance, and the failure state curve, M_f , is the dividing line of failure. Characteristic and failure state curves are the exponent function of mean stress in Eq. (17) and Eq. (18) as follows:

$$M_c = M(p/p_c)^n \quad (17)$$

$$M_f = M(p/p_c)^{-n} \quad (18)$$

where n is the material parameter and p_c is the reference crushing stress. Three curves start from the origin point O and intersect at point D again. The reference crushing stress, p_c , is fixed as the horizontal coordinate of point D . Straight lines AB , CD and EF represent the stress path on the p - q plane. Along the horizontal axis, p_{oA} is the relative low confining pressure and p_{oC} and p_{oE} are the medium and high confining pressures, respectively.

Path AB : During this loading process, two phases exit, changing at point K . On the path AK , the soil volume contracts (negative dilatancy) and then expands (positive dilatancy) during path KB .

Path CD : The characteristic state changes and failure happens at the same time. The soil volume contracts during the entire loading process. The final stage is negative dilatancy.

Path EF : When loading begins, the soil volume will contract constantly until failure occurs. Failure occurs before the characteristic state changes because the stress path reaches the failure line earlier before it reaches the characteristic state change line.

This theoretical model can thus predict the change from negative to positive dilatancy of dense soil when it is subjected to low confining pressure and negative dilatancy once the confining pressure is high.

Generally, there are seven parameters in this constitutive model for sand with crushing. The Poisson ratio, ν , is assumed to be 0.3. The parameters of the constitutive model and the joint element, discussed next, are given in Table 2. The parameter, C_i is the compression index and C_e is the swelling index. The validity of the constitutive model is examined in Yao *et al.* (2008b). The predicted values of the constitutive model for sand with crushing are compared with the experimental results of a triaxial high compression test with variable confining pressures and show good agreement. The experimental results refer to the conventional triaxial compression test performed by Sun *et al.* (2007). The specimen in those tests was Toyoura sand with a relative density of 90%. Drained triaxial compression test has also been performed with confining pressures of 0.2 MPa, 0.5 MPa, 1 MPa, 2 MPa, 4 MPa and 8 MPa.

Table 2 The model parameters with sand crushing and joint elements (Uesugi and Kishida (1986), Yao *et al.* (2008b))

Joint model	Crushing model		
	Triaxial compression	Isotropic consolidation	Poisson ratio
$K_s = 300N/cm^3$	$M = 1.35$	$C_i = 0.0044$	
$K_c = 10^5 N/cm^3$	$n = 0.085$	$C_e = 0.0016$	$\nu = 0.3$
$\mu = 0.45$	$p_c = 5.85 MPa$	$m = 0.5$	

4.1.3 Elasto-plastic constitutive tensor

The constitutive tensor, D_{ijkl}^{ep} , for the incremental general form of the constitutive model in Eq. (19), is derived here. It will be used in the matrix form of the governing equations for efficient solving in FEM.

$$D_{ijkl}^{ep} = L\delta_{ij}\delta_{kl} + G(\delta_{ik}\delta_{jl} + \delta_{il}\delta_{jk}) - \left(L \frac{\partial f}{\partial \sigma_{pp}} \delta_{ij} + 2G \frac{\partial f}{\partial \sigma_{ij}} \right) \left(L \frac{\partial f}{\partial \sigma_{qq}} \delta_{kl} + 2G \frac{\partial f}{\partial \sigma_{kl}} \right) / X \tag{19}$$

where

$$X = \frac{M_c^4 M_f^4 - \eta^4}{M_f^4 M_c^4 - \eta^4} \frac{\partial f}{\partial \sigma_{ij}} \delta_{ij} + \frac{\partial f}{\partial \sigma_{ij}} D_{ijkl}^e \frac{\partial f}{\partial \sigma_{kl}} \tag{20}$$

where G and L are Lamé’s constants from Eq. (21) and Eq. (22), f is the yield function of the model for sand with crushing, η is the ratio of deviatoric stress to the mean stress and δ_{ij} is the Kronecker delta.

$$G = \frac{E}{2(1 + \nu)} = \frac{3(1 - 2\nu)p_a^m}{2mC_e p^{m-1}(1 + \nu)} \tag{21}$$

$$L = \frac{E}{3(1 - 2\nu)} - \frac{2}{3}G = \frac{p_a^m}{mC_e p^{m-1}} - \frac{2}{3}G \tag{22}$$

where E and ν are the elastic modulus and Poisson’s ratio, respectively. m is the material parameter for sand.

4.2 Joint element model

It is well known that interfaces often play a major role in the mechanical behavior of structures interacting with soil. The soil-pile interaction is typical in that the soil is in contact with the engineered structure. In this study, the emphasis is on the contact behavior between the sand and the pile. Consequently, it is necessary to

employ a suitable constitutive relationship to model the heavily loaded interacting region.

A number of models have been presented to describe the interface behavior between the soil and a rigid structure. Among them, Goodman *et al.* (1968) was the pioneer in establishing the constitutive modeling at the interface or at the rock joints. The four-node joint element with zero-thickness assumes a linear relationship between the stress and the relative displacement at the interface in Eq. (23) as follows:

$$\begin{Bmatrix} f_s \\ \sigma_c \end{Bmatrix} = \begin{bmatrix} k_s & 0 \\ 0 & k_c \end{bmatrix} \begin{Bmatrix} \Delta u \\ \Delta v \end{Bmatrix} \tag{23}$$

The model for the joint element is shown in Figure 4.

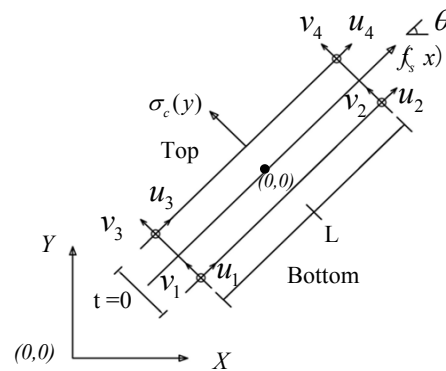


Figure 4 Concept of joint element

In Eq. (23), f_s is the shear stress, σ_c is the compression stress, k_c and k_s are the tangential and normal stiffness per unit length along the interface, respectively, and Δu and Δv represent tangential and normal relative displacement, respectively. The line 1-3 and line 2-4 are straight lines. The nodes 1 and 3, 2 and 4 are in coincident position before deformation. In the finite element analysis, node 1 and 3, 2 and 4 employ the same coordinates. They can be approximated by using linear interpolation functions N_1 and N_2 in Eq. (24), where $N_1 = 1 - 2x/L$ and $N_2 = 1 + 2x/L$. Horizontal and vertical nodal displacements are expressed as

$$\{u\} = \{u_1 \ 0 \ u_2 \ 0 \ u_3 \ 0 \ u_4 \ 0\}^T \text{ and } \{v\} = \{0 \ v_1 \ 0 \ v_2 \ 0 \ v_3 \ 0 \ v_4\}^T$$

$$\{w\} = \begin{Bmatrix} \Delta u \\ \Delta v \end{Bmatrix} = \begin{Bmatrix} w_s^{top} - w_s^{bottom} \\ w_n^{top} - w_n^{bottom} \end{Bmatrix} = \frac{1}{2} \begin{bmatrix} -N_1 & 0 & -N_2 & 0 & N_2 & 0 & N_1 & 0 \\ 0 & -N_1 & 0 & -N_2 & 0 & N_2 & 0 & N_1 \end{bmatrix} \begin{Bmatrix} u \\ v \end{Bmatrix} \tag{24}$$

The special rule, shown in Figure 5, is needed to identify the four modes of joint element deformation, i.e., contact, slip, de-bonding and re-bonding, described by Li (1993). In the contact mode, if the shear stress, k_s , reaches the yield stress, k_{rs} , the sliding condition is assumed to be controlled by the Mohr-Coulomb failure criterion and slip occurs. The value of k_s is equal to k_{rs} if slip occurs. For simplicity, the relationship of the joint element can be assumed to be perfect elasto-plastic (k_{rs} is equal to 0). In the mode of de-bonding and re-bonding, if the normal stress, σ_c , is tensile, the coefficients k_s and k_c are equal to zero. The parameters of the joint element are adapted from the experiments performed by Uesugi and Kishida (1986) and Uesugi and Kishida (1988). The three parameters are given in Table 2, where μ is the friction coefficient.

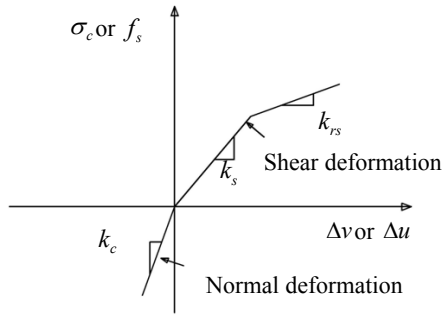


Figure 5 Constitutive relationship of joint element

The local coordinate system, (x,y) , can be directly converted into the global coordinate system, (X,Y) , using a transformation matrix consisting of the rotation angle θ , shown in Eq. (25). The joint elements are placed at the interface between soil and the pile.

$$\begin{bmatrix} x \\ y \end{bmatrix} = \begin{bmatrix} \cos\theta & \sin\theta \\ -\sin\theta & \cos\theta \end{bmatrix} \begin{bmatrix} X \\ Y \end{bmatrix} \quad (25)$$

4.3 Preparation for numerical analysis

Pile is generally modeled as an axisymmetric structure for analytical convenience. The entire analysis area is the model ground tank container, 300 mm radially and 550 mm high, as shown in Figure 6 (a). The surcharge pressures acting on the upper surface of the model ground simulate the actual soil stress at different depths. The boundary-constrained condition for the model ground is set to correspond to the model pile loading test setup. The basic physical features of Toyoura sand in the triaxial compression test and the ground material in the model pile loading tests are the same as the specimen material test performed by Sun *et al.* (2007). Therefore, the values of the seven parameters are deemed reliable for the numerical analysis of the model pile loading test. The mesh for the case of the model pile with a flat base is shown in Figure 6 (b).

The behavior of the sand ground is represented by the constitutive model considering particle crushing. The joint element is applied to simulate the interface behavior during the pile loading process. The joint elements are placed on the pile shaft and the pile tip. For calculation simplicity, the meshing was finished using three nodal triangular elements. The total numbers of triangular elements, joint elements and nodes for different piles are shown in Table 3.

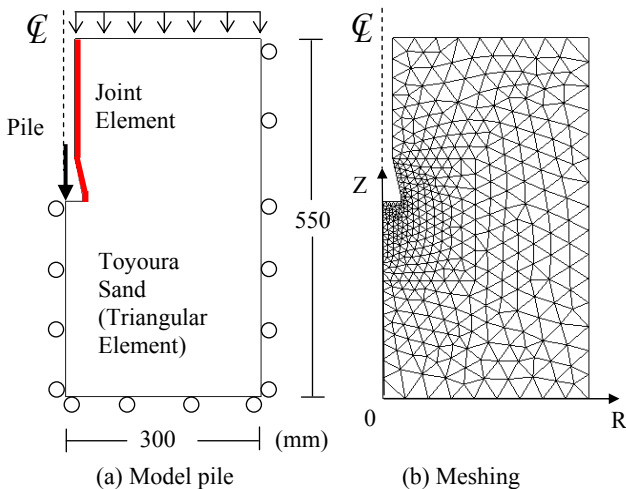


Figure 6 Element meshing

The numerical calculations are conducted using the displacement-controlled method. The displacement control points

are at the bottom of the pile tip and all control points descend simultaneously. The displacement is added by equivalent increments. The final displacement is equal to the shaft diameter of the pile in each calculation step. The influence of the pile installation on the bearing capacity is neglected because the model pile is installed before the model ground is created.

Table 3 Total number of meshing elements for underreamed piles

	Flat Base Pile	Pencil-shaped Base Pile	Pencil-shaped Base Pile
Convergent angle	90	60	30
Triangular element number	822	779	747
Joint element number	18	24	26
Node number	450	428	412

5. RESULTS AND DISCUSSIONS

5.1 The relationship between normalized bearing stress and displacement

The predicted relationships between normalized bearing stress and displacement are compared to experimental results in this study. In the numerical simulation, the pile is pushed into the sandy soil by the prescribed displacements. The vertical reaction forces are summed to the pile tip.

In this study, the normalized bearing stress is defined as the ratio of the current bearing stress at the pile tip to the surcharge pressure. The normalized displacement is often used in analyses, as defined by the ratio of the current displacement (S) to the pile shaft diameter (D). Predicted values using numerical analysis of underreamed piles with flat bases and pencil-shaped bases are compared with experimental results in Figure 7, Figure 8 and Figure 9. The dashed lines show the experimental results, while the solid lines show the predicted values. The convergent angles of the pencil-shaped piles are 60 and 30 degrees.

The predicted values agree well with the experimental results during the entire loading process for each surcharge pressure. The accuracy of the predicted value is especially good when the displacement is small. All the predicted values slightly overestimate the actual test results, as shown in Figures 7, 8 and 9. The predicted discrepancy is less affected by pile shape. The maximum discrepancy between predicted and measured results occurs when surcharge pressure is 400 kPa. Li and Yamamoto (2005) predicted the same relationship using small deformation analysis and the modified Cam Clay model revised using the SMP criterion. The predicted result only agreed with test results when the normalized displacement was smaller than 0.5. The accuracy of the prediction is improved by incorporating the large deformation analysis and mechanical characteristics of the joint element and by using the constitutive model for sand with particle crushing.

The bearing stress of the pile with the enlarged base has been increased during the test. However, the rate of increase of the bearing stress depends on the shape of the enlarged base. The numerical results show that the bearing stress of the underreamed pile decreases as the convergent angle decreases. The normalized bearing stress of the pencil-shaped base pile with a 30-degree convergent angle loses approximately twenty percent at the final state. The confining stress on the soil particles in the area around the pile tip decreases as the convergent angle decreases. Although the surcharge pressure acting on the top surface of the model ground increases, the normalized bearing stress decreases, contrary to the expected trend. This decreasing in the normalized bearing stress is

related to the particle crushing. It can be explained by the high number of sand particles that are crushed under the high surcharge

and 14, respectively. The distribution of radial strain, vertical strain and circumferential strain contours of sand around the underreamed pile are shown in Figures 12, 13 and 15, respectively.

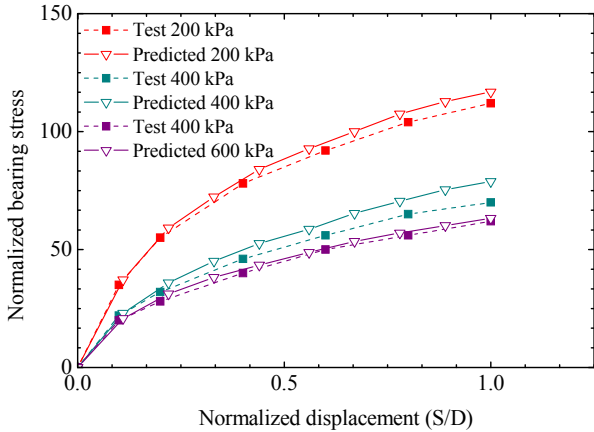


Figure 7 The relationship between normalized bearing stress and normalized displacement ($\alpha=90^\circ$)

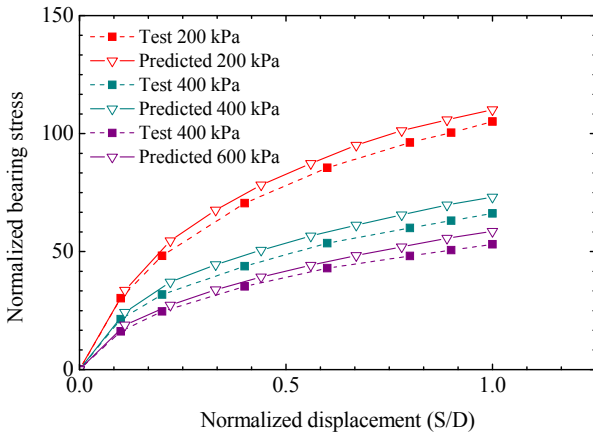


Figure 8 The relationship between normalized bearing stress and normalized displacement ($\alpha=60^\circ$)

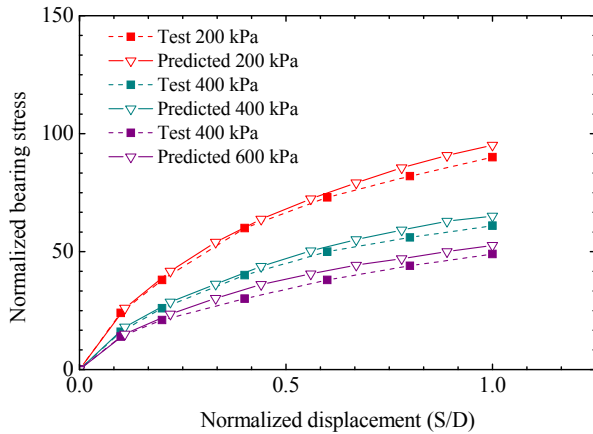
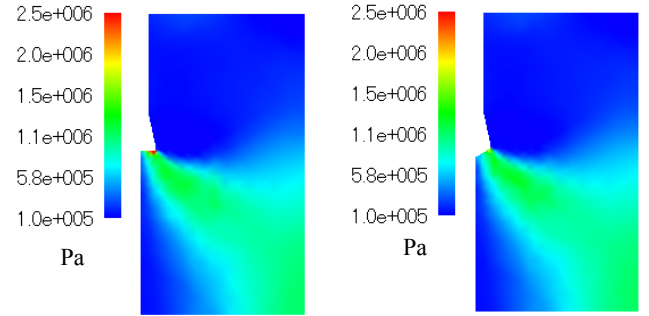


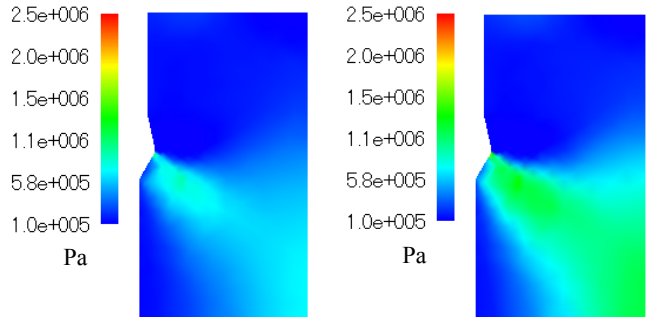
Figure 9 The relationship between normalized bearing stress and normalized displacement ($\alpha=30^\circ$)

5.2 Distribution of stress and strain contours

The visualization of the stress and strain contours helps in understanding the soil behavior when pile is jacked into sandy soil. Dijkstra *et al.* (2009) also implemented the axisymmetric analysis of pile installation in both loose and dense sand layers. The distribution of radial stress, vertical stress and circumferential stress contours in the sand around the underreamed pile are shown in Figures 10, 11

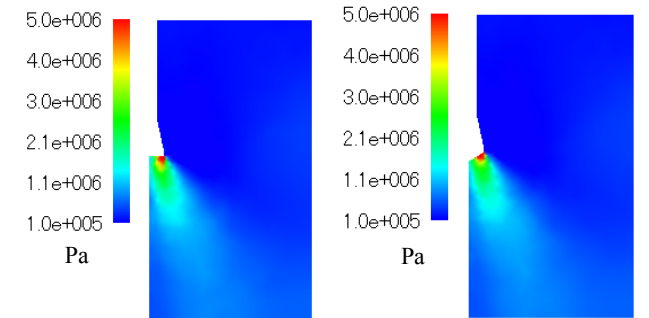


(a) $S/D=1.0 \alpha=90^\circ$ (b) $S/D=1.0 \alpha=60^\circ$

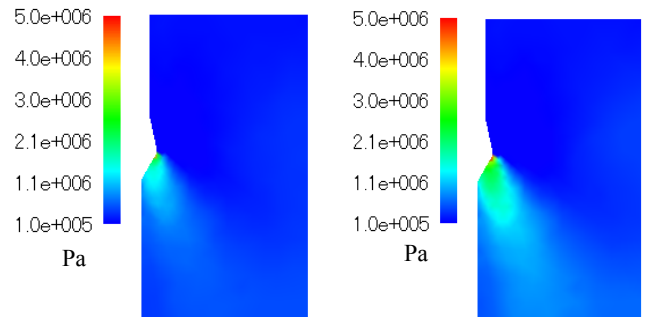


(c) $S/D=0.5 \alpha=30^\circ$ (d) $S/D=1.0 \alpha=30^\circ$

Figure 10 The radial stress contours (Surcharge Pressure 200 kPa)

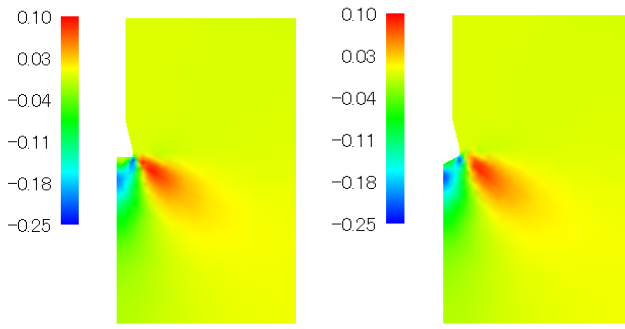


(a) $S/D=1.0 \alpha=90^\circ$ (b) $S/D=1.0 \alpha=60^\circ$



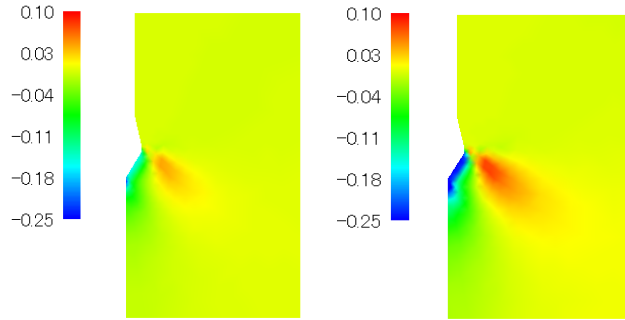
(c) $S/D=0.5 \alpha=30^\circ$ (d) $S/D=1.0 \alpha=30^\circ$

Figure 11 The vertical stress contours (Surcharge Pressure 200 kPa) Pressure



(a) $S/D=1.0 \alpha=90^\circ$

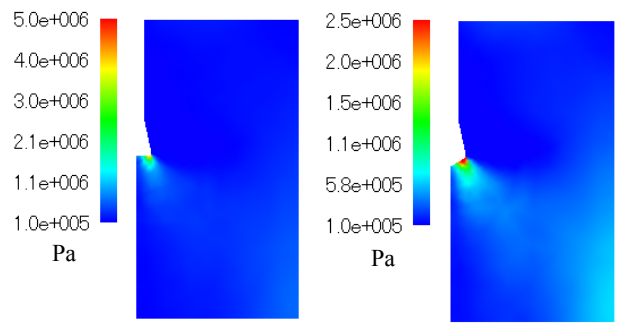
(b) $S/D=1.0 \alpha=60^\circ$



(c) $S/D=0.5 \alpha=30^\circ$

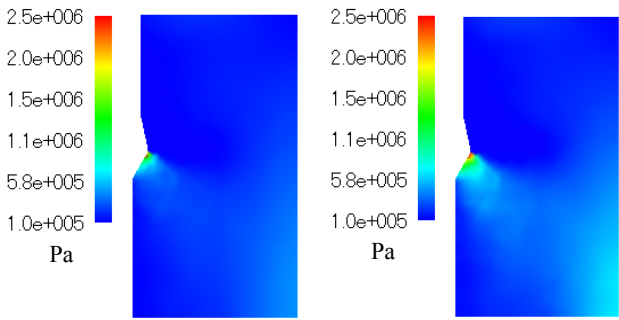
(d) $S/D=1.0 \alpha=30^\circ$

Figure 12 The radial strain contours (Surcharge Pressure 200 kPa)



(a) $S/D=1.0 \alpha=90^\circ$

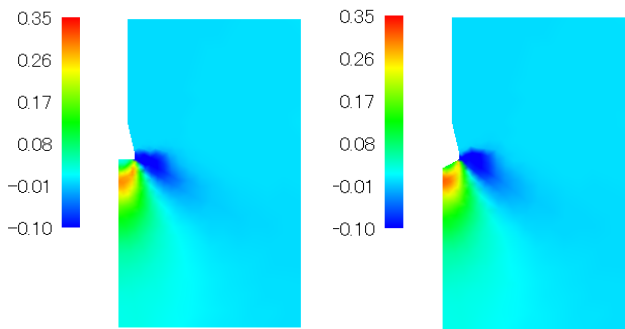
(b) $S/D=1.0 \alpha=60^\circ$



(c) $S/D=0.5 \alpha=30^\circ$

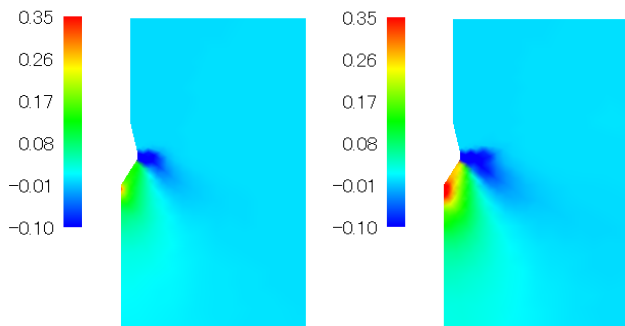
(d) $S/D=1.0 \alpha=30^\circ$

Figure 14 The circumferential stress contours (Surcharge Pressure 200 kPa)



(a) $S/D=1.0 \alpha=90^\circ$

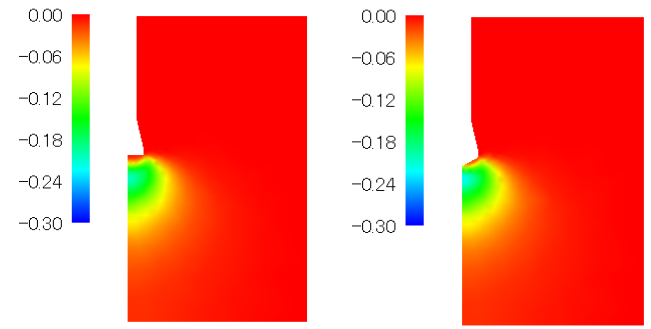
(b) $S/D=1.0 \alpha=60^\circ$



(c) $S/D=0.5 \alpha=30^\circ$

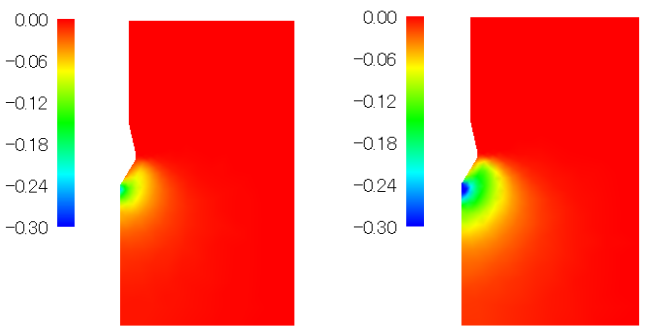
(d) $S/D=1.0 \alpha=30^\circ$

Figure 13 The vertical strain contours (Surcharge Pressure 200 kPa)



(a) $S/D=1.0 \alpha=90^\circ$

(b) $S/D=1.0 \alpha=60^\circ$



(c) $S/D=0.5 \alpha=30^\circ$

(d) $S/D=1.0 \alpha=30^\circ$

Figure 15 The circumferential strain contours (Surcharge Pressure 200 kPa)

In this study, (a), (b) and (d) in each figure represent the distribution of stress or strain contours of pile with convergent angles of 90, 60 and 30 degrees. The stress and strain contours are shown for the pile penetrating at different depths for the same surcharge pressure level as well. The normalized displacement reaches 0.5 and 1.0 in (c) and (d) in each case. The initial surcharge pressure, 200 kPa, is given to all the elements of the model ground in the vertical direction. The lateral coefficient is set as 0.5. The compressive direction is taken as the positive in all the stress and strain contours. The maximum radial stress first occurs at the corner of the pile base in Figure 10 (a). The pile base was made of mortar, and crack failure was observed on the surface of the flat base of the pile in Figure 16 (a) when the tests were completed. Once crack failure occurs in the pile base, the bearing capacity of the pile decreases. The results in Figure 10 (a) and Figure 10 (d) show that the radial stress around the pile with the pencil-shaped base is smaller than that of the pile with the flat base. The underreamed pile with the pencil-shaped base is capable of preventing crack failure, as shown in Figure 16 (b). The crack failure in this case is explained as the result of significant radial stress acting on the pile base when the pile base shape is flat.

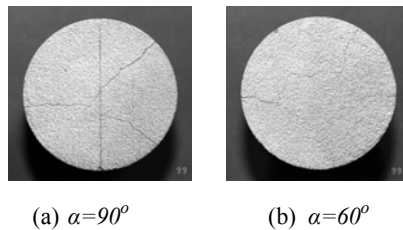


Figure 16 Crack failure on the surface of two pile bases (Surcharge pressure 200 kPa) (Yamamoto *et al.* (2003))

The distribution of the vertical stress contours is displayed in Figure 11. The distributed area of high-value vertical stress is approximately three diameter lengths in the vertical down direction and three diameter lengths in the radial direction. The high-value vertical stress concentrates in the corner just beneath the pile base in Figure 11 (a) and Figure 11 (b). The distributed shape of vertical stress contour expands as the pile penetrates deeper in the sand, as observed by comparing Figure 11 (c) with Figure 11 (d). The range of the high-value vertical stress decreases markedly as the convergent angle decreases, as shown in Figure 11 (d).

The distributed range of the high-value circumferential stress is one diameter length in the vertical down direction and one diameter length in the radial direction, as shown in Figure 14. The distributed area of the high-value circumferential stress is less affected by the pile tip shape. By comparing the distribution of stress contours in Figures 10 (c) and 10 (d), Figures 11 (c) and 11 (d) and Figures 14 (c) and 14 (d), the distributed area of the high-value stress contour expands in both the vertical down and radial direction as the driving depth increases.

The high negative-value radial strain contours are just beneath the pile tip. In addition, the region of the high negative-value radial strain expands as the convergent angle decreases, as seen by comparing Figures 12 (a) and 12 (d). The high negative-value radial region is concentrated two diameter lengths in the vertical down direction. The non-irregular elliptic distribution of the high positive-value radial strain counter is located in the corner of the pile base. The results show that the volumetric expansion beneath the pile tip turns to volumetric compression in the corner of the pile base. Such a tendency is compatible with the predicted result by Sheng *et al.* (2008). The distributed area of the high positive-value radial strain is not influenced very much by the shape of the pile tip.

The high positive-value vertical strain is beneath the pile tip, four diameter lengths deep, as shown in Figures 13 (a), 13(b) and 13(d). The soil particles in this area are heavily compressed. The size of the distributed area of the high positive-value vertical strain increases as the convergent angle becomes smaller. However, the

high negative-value distributed shape becomes smaller as the convergent angle becomes smaller. The high negative-value vertical strain appears around the corner of the pile base and the distributed irregular shape is not influenced by the convergent angle.

The distributions of circumferential strain contour are shown in Figure 15. The shape of the distribution of circumferential strain is elliptical. The area of the distributed elliptical shape is one diameter length in the vertical down direction and two diameter lengths in the radial direction. The minimum negative-value circumferential strain appears in Figure 15 (d) for the underreamed pile with a 30-degree convergent angle. The distributed shape of the high negative-value circumferential strain is affected by the pile tip shape. Moreover, the distribution of the high-value strain contours expand in both the vertical down and the radial direction with larger penetrating depth, as shown in Figures 12 (c) and 12 (d), Figures 13 (c) and 13 (d) and Figures 15 (c) and 15 (d).

5.3 The stress-strain relationship at different depths beneath pile tip

To investigate the soil behavior variance of elements at different depths and to emphasize the necessity of applying the constitutive model with particle crushing in numerical computations, three elements at different depths beneath the pile tip are selected and their mechanical behavior relationships are demonstrated. The outline of the model ground and the three elements numbered 49, 89 and 405 are shown in Figure 17. Figure 18 shows the relationship between the stress ratio and deviatoric strain under different surcharge pressures for these three elements. Sub-titles (a), (b) and (c) of each figure indicate the predicted values of the mechanical relationship for element No. 49, No. 89 and No. 405, respectively.

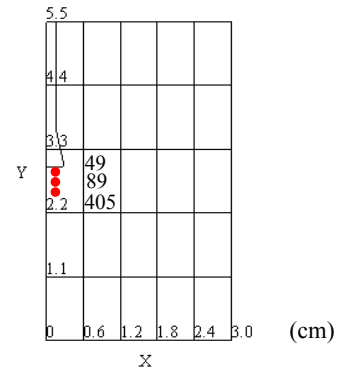


Figure 17 Three elements beneath pile base at different depths

The stress ratio is defined as the ratio of the mean stress to the deviatoric stress. The stress ratio decreases as the surcharge pressure increases at a single element. Figure 18 (a), 18 (b) and 18 (c) show that the stress ratio increases with increasing depth beneath the pile tip with the same surcharge pressure level. The initial stress ratio is 0.75 because the lateral coefficient is assumed to be 0.5, as in previous. The predicted results show that the deviatoric strain of element No. 89 is larger than that of the other two elements because element No. 89 is in the region of significant shear beneath the pile tip. The predicted relationship between the volumetric strain and the deviatoric strain are shown in Figure 19. The volume contraction and expansion of the element at different depths are reasonably demonstrated by the predicted values, as shown in Figure 19. In Figure 19 (a), the volume of the element No. 49, in the significant compressive region, shrinks under all three levels of surcharge pressure. The volume contraction is from the particle crushing and rearrangement. The degree of volume reduction increases with increasing surcharge pressure. The volume of element No. 89 contracts initially, and then expands when the surcharge pressure reaches 200 kPa. The only volumetric contraction of element No. 89 is observed when the 400 kPa and the 600 kPa surcharge pressure are applied, as shown in Figure 19 (b).

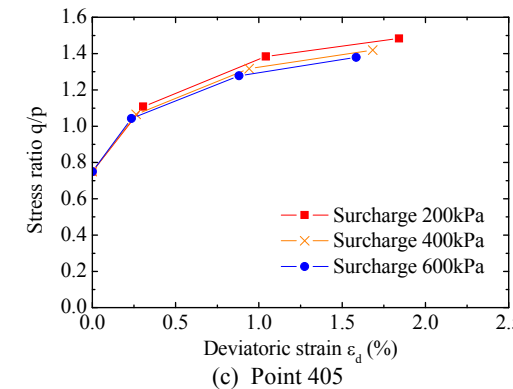
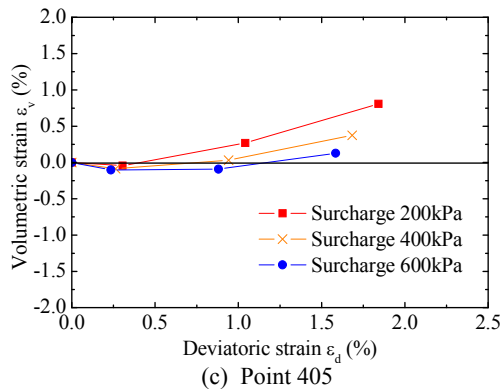
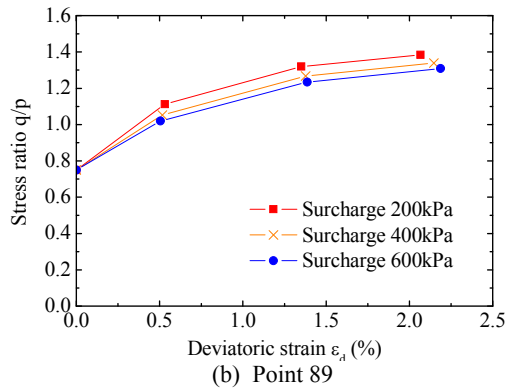
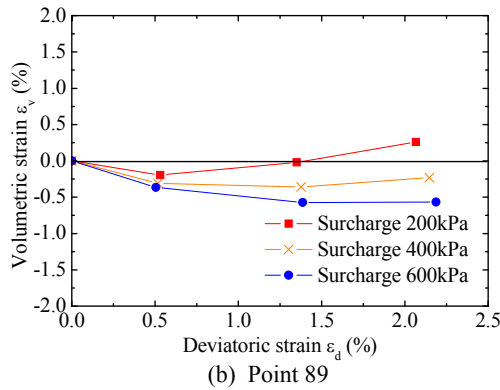
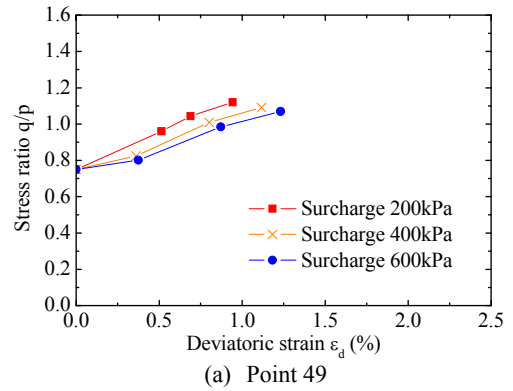
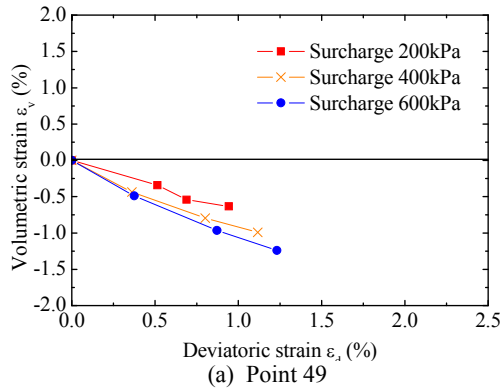


Figure 19 The relationship between the volumetric strain and the deviatoric strain of the elements at different depth beneath pile tip

Figure 18 The relationship between the stress ratio and the deviatoric strain of the elements at different depth beneath pile tip

The volume expansion of element No. 405 is predicted under all three surcharge pressures, as shown in Figure 19 (c). The degree of positive dilatancy becomes more noticeable as the surcharge pressure decreases. The markedly positive dilatancy tendency shown in the model means that the confining pressure on element No. 405 is weakened. The soil elements at different depths or positions beneath the pile base may experience various volumetric changes. Consequently, it is important to integrate the constitutive model for sand with particle crushing with finite element analysis of the model pile loading test. The extent of the volume contraction is not quite distinctive of element No. 49 in Figure 19 (a) and can also be attributed to the stress condition of the soil behavior just beneath the pile base, which may differ from that measured in the triaxial compression test.

6. CONCLUSIONS

To investigate the effect of pile tip shape on soil behavior around a pile, the application of finite element analysis is presented that incorporates the mixed incremental method for the UL method and the characteristics of particle crushing. The major findings of the study are summarized below.

- (1) The predicted values of the relationship between normalized bearing stress and normalized displacement of underreamed model piles agreed with the experimental results.
- (2) The distribution of stress contours: The distribution area of the high radial stress contours around the underreamed pile increases as the convergent angle decreases. A significant finding is that an underreamed pile with a smaller convergent angle can prevent crack failure on the pile base surface. The distributed area of the high-value vertical stress contour is approximately three diameter lengths in the vertical down direction and three diameter lengths in the radial direction. The high-value vertical stress concentrates in the corner just beneath the pile base and decreases as the convergent angle decreases to 30 degrees. The distributed area of high-value circumferential stress is less affected by the shape of the pile tip.
- (3) The distribution of strain contours: The negative-value radial strain contours are just beneath the pile tip. In addition, the distributed region of the high negative-value radial strain expands as the convergent angle decreases. The distributed area of the high positive-value vertical strain develops beneath the pile tip and becomes more significant for the underreamed pile with a 30-degree convergent angle. The high negative-value

vertical strain appears around the corner of the pile base, and its distributed shape is not influenced by the convergent angle. The distributed shape of the high negative-value circumferential strain is affected by the shape of the pile tip.

- (4) The mechanical behavior of elements beneath the pile tip at different depths is examined. The predicted relationship between the stress ratio and the deviatoric strain shows that the stress ratio variances for the three elements exhibit nearly the same tendency. The stress ratio decreases with increasing surcharge pressure for the same element. When the position of the element is closer to the pile base, the stress ratio decreases. However, the volumetric contraction is remarkable. Three elements display different volume variation close to real behavior. Consequently, it is vital to integrate the constitutive model for sand with particle crushing into finite element analysis of the model pile loading test.

The numerical analysis presented in this paper can be improved in some aspects. For example, the interface element between the pile and the surrounding soil is very simple; the experimental technology to measure frictional coefficient for interface model needs further investigation; a more advantageous model that is capable of predicting dilatancy and strength softening should be incorporated in the numerical analysis in further work. Additionally, the effects of parameter for constitutive model on the predicted results of pile loading in sandy soil will be examined in further study.

7. REFERENCES

Chen, W. F. and Mizuno, E. (1990) "Nonlinear analysis in soil mechanics: Theory and Implementation". Netherlands, ELSEVIER, pp 492-504.

Cooke, R. W., and Whitaker, T. (1961) "Experiments on model piles with enlarged bases". *Geotechnique*, 11(1), pp1-13.

Dauouadji, A., Hicher, P. Y. and Rahma, A. (2001) "An elastoplastic model for granular materials taking into account grain breakage". *European Journal of Mechanics a-Solids*, 20(1), pp 113-137.

Dauouadji, A. and Hicher, P. Y. (2010) "An enhanced constitutive model for crushable granular materials". *International Journal for Numerical and Analytical Methods in Geomechanics*, 34(6), pp 555-580.

Dijkstra, J., Broere, W. and Heeres, O. M. (2009) "Numerical simulation of pile installation". *Computers and Geotechnics*, 38(5), pp 612-622.

Fukumoto, T. (1992) "Particle breakage characteristics of granular soils". *Soils and Foundations*, 32(1), pp 26-40.

Gadala, M. S., Dokainish, M. A. and Oravas, G. AE. (1984) "Formulation methods of geometric and material nonlinearity problems". *International Journal for Numerical and Analytical Methods in Engineering*, 20(5), pp 887-914.

Gennaro, V. D., Frank, R. and Said, I. (2008) "Finite element analysis of model piles axially loaded in sands". *Rivista Italiana di Geotecnica*, 2, pp 63-90.

Goodman, R.E., and Taylor, R. L. (1968) "A model for the mechanics of jointed rock". *Journal of the Soil Mechanics and Foundation Division*, 94(SM3), pp 637-659.

Hardin, B. (1985) "Crushing of soil particles". *Journal of Geotechnical Engineering*, 111(10), pp 1177-1192.

Hibbitt, H. D., Marcal, P.V. and Rice, J. R. (1970) "A finite element Formulation for problems of large strain and large displacement". *International Journal of Solids and Structures*, 6(8), pp1069-1086.

Hu, W., Yin, Z. Y. and Dano, C. and Hicher, P. Y. (2011) "A constitutive model for granular materials considering grain breakage". *Science China Technological Sciences*, 54(8), pp 2188-2196.

Hu, Y., and Randolph, M. F. (1998a) "A practical numerical approach for large deformation problems in soil". *International Journal for Numerical and Analytical Methods in Geomechanics*, 22(5), pp 327-350.

Hu, Y., and Randolph, M. F. (1998b) "H-adaptive FE analysis of elasto-plastic non-homogeneous soil with large deformation". *Computers and Geotechnics*, 23(1), pp 61-83.

Ishikawa, K., Ito, A. and Ogura, H. (2011) "Effect of tip length and strength of enlarged grouted base on bearing capacity of straight pile, Part 1". *Journal of Structure and Engineering*, 76, pp 2017-2113.

Ishikawa, K., Ito, A. and Ogura, H. (2012) "Effect of tip length and strength of enlarged grouted base on bearing capacity of straight pile, Part 2". *Journal of Structure and Engineering*, 77, pp 883-889.

Keji, K., Masayuki, H. and Adrian F.L.H. (2009) "Pile Bearing Capacity Factors and Soil Crushability". *Journal of Geotechnical and Geoenvironmental Engineering*, 135(7), pp 901-913.

Kim, H. J., Mission, J. L.C. and Park, S. (2007) "Analysis of Static Axial Load Capacity of Single Piles and Large Diameter shafts using Nonlinear Load Transfer Curves". *KSCE Journal of Civil Engineering*, 11(6), pp 285-292.

Kikumoto, M., Wood, D. M. and Russell, A. (2010) "Particle crushing and deformation behaviour". *Soils and Foundations*, 50(4), pp 547-563.

Kiouis, P. D., Voyiadjis, G. Z. and Tumay, M.T. (1988) "A Large strain theory and its application in the analysis of the cone penetration mechanism". *International Journal for Numerical and Analytical Methods in Geomechanics*, 12, pp 45-60.

Lade, P. V., Yamamuro, J. A. and Bopp, P. A. (1996) "Significance of particle crushing in granular materials". *Journal of Geotechnical and Geoenvironmental Engineering*, 122(4), pp 309-316.

Li, J. C. (1993) "Numerical Simulation of interfaces in Geomechanics: Development of New Zero-thickness Interface Elements". Doctor thesis for University of Delaware, pp 3-14.

Li, W., and Yamamoto, H. (2005) "Numerical analysis on soil behavior around pile-tip under vertical load". *Structure and Construction of Proceeding of Japan Architecture*, 51(B), pp 147-157. (In Japanese)

Lobo-Guerrero, S., and Vallejo, L. E. (2007) "Influence of pile shape and pile interaction on the crushable behaviour of granular materials around driven piles: DEM analyses". *Granular Matter*, 9(3-4), pp 241-250.

Martin, R. E., and Desteph, R. (1983) "Large diameter double Underreamed drilled shafts". *Journal of Geotechnical Engineering*, 109(8), pp 1082-1098.

Miura, N., and Yamamouchi, T. (1977) "Effect of particle-crushing on the shear characteristics of a sand". *Proceeding of Japan Society of Civil Engineering*, 260, pp 109-118. (In Japanese)

Miura, N., Murata, H. and Yasufuku, N. (1984) "Stress-strain characteristics of sand in a particle-crushing region". *Soils and Foundations*, 24(1), pp 77-89.

Nazem, M., Sheng, D. C. and Carter, J. P. (2006) "Stress integration and mesh refinement for large deformation in geomechanics". *International Journal for Numerical Method in Engineering*, 65(7), pp 1002-1027.

Nazem, M., Sheng, D. C., Carter, J. P. and Sloan, S. W. (2008) "Arbitrary Lagrangian-Eulerian method for large-strain consolidation problems". *International Journal for numerical and methods in geomechanics*, 32(9), pp 1023-1050.

Nazem, M., Carter, J.P. and Airey, D. (2009) "Arbitrary lagrangian-Eulerian method for dynamic analysis of geomechanical problems". *Computers and Geotechnics*, 36(4), pp 579-557.

- Nazem, M., Cater, J. P. and Airey, D. W. (2010) "Arbitrary lagrangian-Eulerian method for non-linear problem of geomechanics". Proceeding of the 9th World Congress on Computational Mechanics and 4th Asian Pacific Congress on Computational Mechanics, Sydney, 10, pp 1-10.
- Qiu, G., Henke, S. and Grabe, J. (2011a) "Application of a coupled Eulerian-Lagrangian approach on geomechanical problems involving large deformations", *Computers and Geotechnics*, 38(1), pp 30-39.
- Qiu, G., and Henke, S. (2011b) "Controlled installation of spudcan foundations on loose sand overlying weak clay". *Marine Structures*, 24, pp 528-550.
- Qiu, G., and Grade, J. (2012) "Numerical investigation of bearing capacity due to spudcan penetration in sand overlying clay". *Canadian Geotechnical Journal*, 49(12), pp 1393-1407.
- Roscoe, K. H., and Burland, J. B. (1968) "On the generalised stress-strain behaviour of "Wet" clay". Heyman J., Leckie F.A. *Engineering Plasticity*, Cambridge University Press, pp 535-609.
- Said, I., Gennaro, V. D. and Frank, R. (2009) "Axisymmetric finite element analysis of pile loading tests". *Computers and Geotechnics*, 36(1), pp 6-19.
- Sheng, D. C., Eigenbrod, K. D. and Wriggers, P. (2005) "Finite element analysis of pile installation using large-slip frictional contact". *Computers and Geotechnics*, 32(1), pp 17-26.
- Sheng, D. C., Yamamoto, H. and Wriggers, P. (2008) "Finite element analysis of enlarged end piles using frictional contact". *Soils and Foundations*, 48(1), pp 1-14.
- Sheng, D. C., Nazem, M. and Carter, J. P. (2009) "Some computational aspects for solving deep penetration problems in geomechanics". *Computational Mechanics*, 44(4), pp 549-561.
- Simonini, P. (1996) "Analysis of behavior of sand surrounding pile tips". *Journal of Geotechnical and Geoenvironmental Engineering*, 122(11), pp 897-905.
- Sun, D. A., Huang, W. X., Sheng, D.C. and Yamamoto, H. (2007) "An elastoplastic model for granular materials exhibiting particle crushing". *Key Engineering Materials*, 41, pp 1273-1278.
- Uesugi, M., and Kishida H. (1986) "Influential Factors of friction between Steel and Dry sands". *Soils and Foundations*, 26(2), pp 33-46.
- Uesugi, M., and Kishida, H. (1988) "Behavior of sand particles in sand-steel friction". *Soils and Foundations*, 28(1), pp 107-118.
- Vavourakis, V., Loukidis, D., Charmpis, D. C. and Papanastasiou, p. (2013) "Assessment of remeshing and remapping strategies for large deformation elastoplastic Finite element analysis". *Computers and Structures*, 144, pp 133-146.
- Vesic, A. S. and Clough, G.W. (1968) "Behaviour of granular materials under high stresses". *Journal of the Soil Mechanics and Foundations Division*, 94(SM3), pp 661-688.
- Wu, Y., Yamamoto, H. and Yao, Y. P. (2013) "Numerical study on bearing behavior of pile considering sand particle crushing", *Geomechanics and Engineering, An international journal*, 5(3), pp 241-261.
- Yamamoto, H., Li, W., Tominaga, K. and Ogura, H. (2003) "Experiment study on effects of overburdening pressures and end shapes for point bearing capacities of pile". *Structure and construction of proceeding of Japan Architecture*, 49(B), pp 157-162. (In Japanese)
- Yang, J., Tham, L. G., Lee, P. K. K., Chan, S. T. and Yu, F. (2006) "Behavior of jacked and driven piles in sandy soil". *Geotechnique*, 56(4), pp 245-259.
- Yang, J., and Mu, F. (2008) "Use of State-Dependent Strength in Estimating End Bearing Capacity of Piles in Sand". *Journal of Geotechnical and Geoenvironmental Engineering*, 134(7), pp 1010-1014.
- Yao, Y. P., Sun, D. A. and Matsuoka, H. (2008a) "A unified constitutive model for both clay and sand with hardening parameter independent on stress path". *Computers and Geotechnics*, 35(2), pp 210-222.
- Yao, Y. P., Yamamoto, H. and Wang, N. D. (2008b) "Constitutive model considering sand crushing". *Soils and Foundations*, 48(4), pp 603-608.
- Yasufuku, N., and Hyde, A. F. L. (1995) "Pile end-bearing capacity in crushable sands". *Geotechnique*, 45(4), pp 663-676.
- Yasufuku, N., Ochiai, H. and Ohno, S. (2001) "Pile end-bearing capacity of sand related to soil compressibility". *Soils and Foundations*, 41(4), pp 59-71.
- Yu, F., and Yang, J. (2012) "Base Capacity of Open-ended Steel Pipe Piles in Sand". *Journal of Geotechnical and Geoenvironmental Engineering*, 138(9), pp 1116-1128.